Article

Numerical Analysis on Gas Production and Geomechanical Responses of Natural Gas Hydrate Reservoirs

Mingyu Xue, Yuanfang Cheng,* Yang Li, Chuanliang Yan, Zhongying Han, Yong Chen, and Bo Sun

Cite This: *ACS Omega* 2023, 8, 39604−39615

Read Online

ACCESS | Metrics & More | Article Recommendations

ABSTRACT: Natural gas hydrate (NGH) has attracted considerable global attention as a promising energy resource in recent years. To acquire valuable insights into regarding the interplay between mechanical properties and production outcomes during the production, in this study, a fully coupled thermo-hydro-mechanical-chemical (THMC) model based on the geological features of reservoirs in the Shenhu area of the South China Sea (SCS) was developed to analyze the response characteristics of various physical fields within the reservoir during the exploitation. Furthermore, the study examined the influence of mechanical behavior on hydrate exploitation and investigated the effects of varying initial hydrate saturation and seawater depth on production efficiency and reservoir deformation. The simulation results indicated that neglecting the impact of solid mechanics in the analysis of hydrate productivity can result in overestimated results, particularly during the initial production stage. Reservoirs with higher hydrate saturation experience lower initial production rates due to the influence of permeability and capillary force. Moreover, reservoirs with high hydrate saturation exhibit greater compression but lower wellhead subsidence during the long-term development. The impact of seawater depth on production capacity primarily arises from the pressure's influence on the gas−water ratio, where greater seawater depth corresponds to increased reservoir compression and wellhead subsidence.
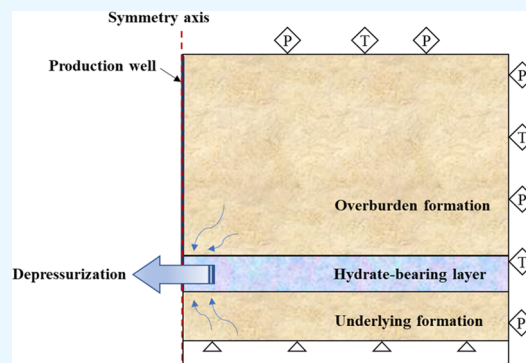
1. INTRODUCTION

NGH is a solid compound composed of methane molecules trapped within a lattice-like structure of water molecules that formed under specific conditions of low temperature and high pressure, typically found in deep-sea sediments and permafrost regions.[1−4] One cubic meter of NGH can release around 160−180 m^3 of natural gas when the hydrate completes decomposition at standard temperature and pressure (STP).[5−7] Compared to other hydrocarbons such as coal and oil, natural gas has a lower carbon content.[8,9] The abundance, widespread global distribution, high energy density, and environmentally cleaner attributes of nature of NGH make it an attractive energy source with significant potential.[10−12] Numerous countries have focused their attention on accelerating its commercialization and recognizing its promising prospects in the energy landscape.

In recent years, significant progress has been made in hydrate mining operations, with notable trials and successful extractions taking place in different regions. Japan conducted two trial mining operations in the Eastern Nankai region in 2013 and 2017.[13−15] In 2017, China conducted its first mining operation in the Shenhu area of the SCS, where it achieved the successful extraction of 3.0 × 10^5 m^3 of methane gas over a period of 60 consecutive days.[16] Building upon this success, China further conducted hydrate horizontal well mining operations in the sea area, resulting in a 30 day extraction period and a cumulative gas production of 8.61 × 10^5 m^3 in 2020.[17,18] These advancements in mining operations provide promising indications that natural methane hydrates can be effectively explored and economically developed in the near future. However, it is crucial to acknowledge that the industry must tackle various geological and engineering obstacles to ensure safe and sustainable extraction in the future.[19−21]

Numerous researchers have undertaken numerical studies aimed at estimating the efficiency of energy exploitation and evaluating the feasibility and production efficiency of NGH production. Zhang et al.[22] established a three-dimensional numerical model to simulate the development of hydrate resources through depressurization using a multibranch well; based on this model, they highlighted that the implementation of a multibranch well is proposed to enhance the recovery efficiency of NGH. They also revealed that the multibranch
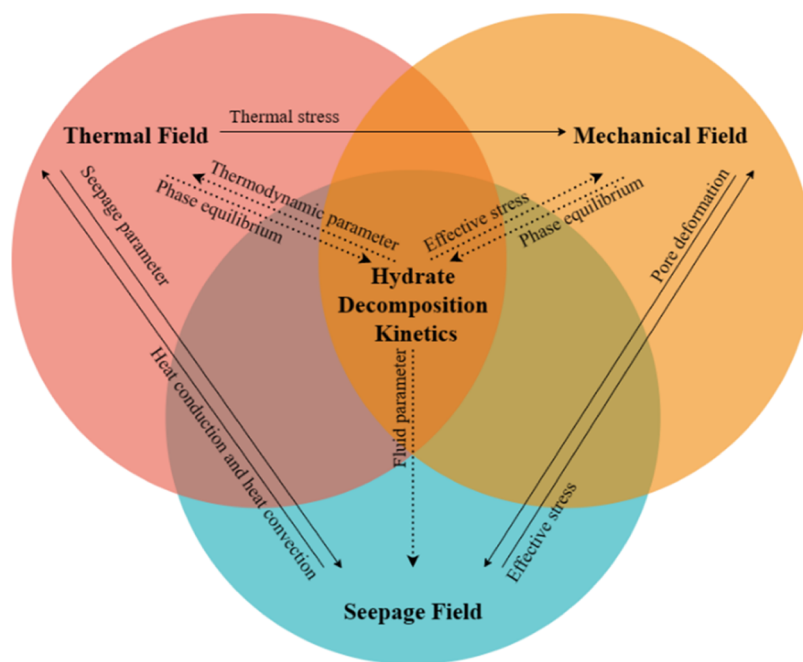
Figure 1. Schematic diagram of a multiphysical field coupling relationship.

well fell short in terms of sustaining gas production over an extended period. Dong et al.[23] developed a three-dimensional (3D) numerical model to simulate gas production from low-permeability NGH reservoirs by using a double-well system. They revealed that compared to a single well, the implementation of the double-well system increased the drainage area and facilitated improved transfer of heat and mass within the NGH formation. Double-well systems exhibit significantly higher gas production rates, ranging from 1.5 to 2.5 times greater. In addition, they observed that an increase in the spacing between the wells improved the overall oil recovery efficiency. Feng et al.[24] put forth a novel approach for enhancing gas production efficiency from NGH reservoirs by combining hydraulic fracturing and depressurization methods. The results indicated that this combination method proved to be more effective in extracting gas compared to the single depressurization method. Additionally, they highlighted the potential of injecting hot water after the fracturing process as a means of enhancing gas production from low-temperature reservoirs.

Their studies have made significant contributions to understanding the behavior of NHG production and offered a promising pathway for optimizing gas production from hydrate formations through numerical techniques. In the process of hydrate production, the decomposition of hydrates will lead to the reduction of formation strength. This may cause the deformation of the strata and even the occurrence of geological disasters, such as submarine landslides and wellbore instability.[25,26] Rutqvist et al.[27] developed the TOUGH + HYDRATE simulator coupled with FLAC to investigate the mechanical properties of the formation during the hydrate decomposition progresses. The results indicated that the increased shear stress and strata deformation around the well were caused by the depressurization. Yoon et al.[28] used the fixed-stress sequential method employed with the TOUGH + HYDRATE and ROCMECH simulators to investigate geomechanical responses of the formation based on various depressurization plans. They revealed that the weak stiffness of

the formation after hydrate dissociation results in significant vertical displacement of the formation, which is likely to intensify as production continues.

However, the impact of considering geomechanical factors on gas production is not well discussed in the earlier studies. The multiphysical responses of hydrate reservoirs to gas production, including thermal, hydraulic, and geomechanical processes, play a crucial role in the overall behavior and stability of the reservoirs. Understanding these responses is essential for assessing the integrity of the reservoir and ensuring the long-term safety and stability of gas production operations.

In this article, we focus on the characteristics of NGH reservoirs in the Shenhu area of the SCS. A numerical simulation model was established to analyze the gas production behavior and the corresponding responses of pressure, temperature, saturation, and geomechanical behavior within hydrate formation during a 600 day period of gas production through depressurization using a single vertical well. Furthermore, by variation of the initial hydrate saturation and seawater depth, an analysis was performed on the gas production rate, reservoir deformation, and wellhead subsidence.

2. METHODOLOGY

2.1. Governing Equations. The process of NGH production is a complex, multiphysics coupling involving various interconnected aspects, such as heat transfer, fluid flow, hydrate dissociation, and solid mechanics, as shown in Figure 1. To accurately model this process, it is crucial to establish the governing equations that describe the multiphysical coupling. In the simulation model, several assumptions are made:

(1) The NGH formation is assumed to be homogeneous and isotropic, with no migration of the solid phase;

(2) The flow of fluids in the formation follows the Darcy's law, and the absolute permeability of the formation is consistent in all directions;
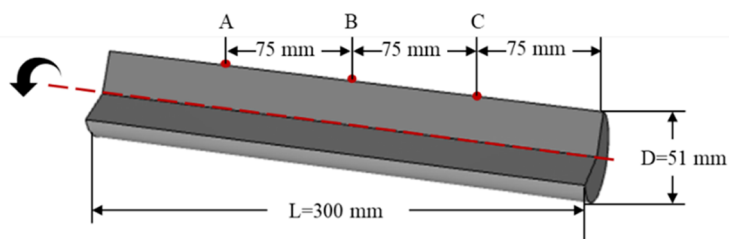
Figure 2. Schematic model of the experiment.

(3) There is no gas dissolution in water and no secondary formation of hydrates.

2.1.1. Mass Conservation Equations. The mass conservation equation of each component in porous media can be expressed as[29,30]

$$\frac{\partial(\phi\rho_i S_i)}{\partial t} = -\nabla\cdot(\phi\rho_i S_i v_i) + \dot{m}_i + q_i \qquad (1)$$

This equation comprehensively considered the influences of the flow of aqueous phase and gaseous phase, temperature change, and rock deformation and used to simulate the flow and migration of various phases within the formation, where ρ_i is the density of component i (i = h, g, w; h, g, w denote the hydrate phase, gaseous phase, and aqueous phase, respectively), S_i, q_i, v_i, $\dot{m}_i$ are the saturation, source-sink term, velocity, and the generation rate of component i; ϕ is the effective porosity of the formation, which can be written as

$$\phi = \frac{1}{1 + \varepsilon_v}(\phi_0 + \varepsilon_v) \qquad (2)$$

where ε_v and ϕ_0 are the volume strain and the initial effective porosity of the formation, respectively.

The hydrate phase has no migration in the porous medium, while the flow velocity expressions of the gaseous phase and aqueous phase can be calculated by Darcy's law:[31−35]

$$v_w = -\frac{Kk_{rw}}{\mu_w}(\nabla P_w + \rho_w g) \qquad (3)$$

$$v_g = -\frac{Kk_{rg}}{\mu_g}(\nabla P_g + \rho_g g) \qquad (4)$$

$$K = K_0(1 - S_h)^N \qquad (5)$$

$$k_{rw} = \left(\frac{\frac{S_w}{1-S_h} - S_{wr}}{1 - S_{wr} - S_{gr}}\right)^{nw} \qquad (6)$$

$$k_{rg} = \left(\frac{\frac{S_g}{1-S_h} - S_{gr}}{1 - S_{wr} - S_{gr}}\right)^{ng} \qquad (7)$$

where K and K_0 are the absolute permeability and the original permeability, while the hydrate saturation is zero of the porous media, respectively; N is the permeability index; g is the gravity force; μ, P, and k are the viscosity, pressure, and the relative permeability of the mobile phase, respectively; S_{wr} and S_{gr} are the residual saturation of aqueous phase and gaseous phase, respectively; nw and ng are the relative permeability index of aqueous phase and gaseous phase, respectively.

2.1.2. Energy Conservation Equations. Hydrate dissociation is a complex endothermic reaction. The energy conservation in this numerical simulation includes heat conduction, heat convection between fluids; heat conduction between fluids and solids as well as the heat absorption by hydrate dissociation can be written as[36−39]

$$\frac{\partial}{\partial t}\rho' C' = \nabla\cdot(\lambda_{eff}\nabla T) - \nabla\cdot(\rho_g C_g v_g + \rho_w C_w v_w) + Q \qquad (8)$$

$$Q = -\dot{m}_h \Delta H \qquad (9)$$

$$\rho' C' = (1 - \phi)\rho_s C_s + \sum \phi S_i \rho_i C_i \qquad (10)$$

$$\Delta H = 446.12 \times 10^3 - 132.638T \qquad (11)$$

$$\lambda_{eff} = (1 - \phi)\lambda_s + \sum \phi S_i \lambda_i \qquad (12)$$

where C_s and C_i are the specific heat of solid and component i; λ_{eff} is the effective heat conductivity coefficient of the formation, λ_s, λ_i are the heat conductivity coefficient of solid and component i, respectively.

2.1.3. Solid Mechanics Equations. Mechanical parameters of formations undergo dynamic changes during the dissociation of NGH. In this paper, the elastic modulus and hydrate saturation are characterized by the linear relation as follows:[40]

$$E_0 = n_s E_s + n_h E_h \qquad (13)$$

where E_0 is the equivalent elastic modulus; n_s and n_h are the volume fraction of reservoir rock and the volume fraction of hydrate, respectively; E_s and E_h are the elastic modulus of formation rock and NGH, respectively.

The effective stress calculation formula of formation is shown as follows:

$$\begin{cases} \overline{\sigma'} = \dfrac{\sigma_1 + \sigma_2 + \sigma_3}{3} - \alpha\delta_{i,j}P - \beta\delta_{i,j}T \\ \delta_{i,j} = 1, \ i = j \\ \delta_{i,j} = 0, \ i \neq j \end{cases} \qquad (14)$$

2.1.4. Natural Gas Hydrate Reaction Kinetics Equation. When the pressure and temperature conditions change, this may lead to hydrate dissociation. The dissociation reaction of hydrates follows the Kim−Bishnoi models, which can be written as[41,42]

$$\dot{m}_g = K_{rd} M_g A_{dec}(P_e - P_g) \qquad (15)$$

$$\dot{m}_h = \dot{m}_g \frac{nM_w + M_g}{M_g} \qquad (16)$$

$$\dot{m}_w = \dot{m}_g \frac{n M_w}{M_g} \tag{17}$$

where K_{rd} is the intrinsic dissociation rate constant; A_{dec} is the total surface area of hydrate decomposition per unit volume; M_g, M_w, M_h are the relative molecular mass of gaseous phase, aqueous phase, and hydrate phase, respectively; $\dot{m}_g$ and $\dot{m}_w$ are the generation rate of gaseous phase and aqueous phase, respectively; $\dot{m}_h$ is the decomposition rate of the hydrate phase; P_e is the phase equilibrium pressure; and n is the decomposition reaction coefficient of the hydrate phase.

2.2. Model Validation. In order to validate the accuracy and assess the reliability and effectiveness of the proposed model, it is crucial to compare the numerical simulation results to experimental data obtained from previous studies. In this case, the seminal experiment conducted by Masuda is widely recognized and can serve as a valuable resource for validating the model.[43,44] This experiment focused on the depressurization-induced dissociation of NGH in the sandstone core samples. A cylindrical sample with a diameter of 51 mm and a length of 300 mm was utilized, as depicted in Figure 2.

The sample was subjected to a consistent water bath temperature of 275.15 K throughout the duration of the experiment. The initial pore pressure was set at 3.75 MPa, and over the course of the experiment, the pressure at the outlet on the right side gradually decreased to 2.84 MPa. Temperature measurements were recorded at three specific points within the sample, identified as A, B, and C. For further details regarding the initial conditions and material parameters pertaining to this experiment, please refer to Table 1[45,46]

Table 1. Main Parameters for Numerical Simulations

parameters	value	parameters	value
initial hydrate saturation	0.501	initial water saturation	0.351
core initial temperature	275.45 K	ambient temperature	275.15 K
absolute permeability	97.98 mD	porosity	0.182
initial pressure	3.75 MPa	core right end pressure	2.84 MPa

Figure 3 presents a comparison between the numerical simulation results and experimental data for temperature measurements at the test points and cumulative gas production at the outlet. It can be observed that the experimental results and numerical simulation results exhibit consistent trends and demonstrate a good level of agreement. The alignment between these two data sets further substantiates the accuracy and reliability of the numerical model.
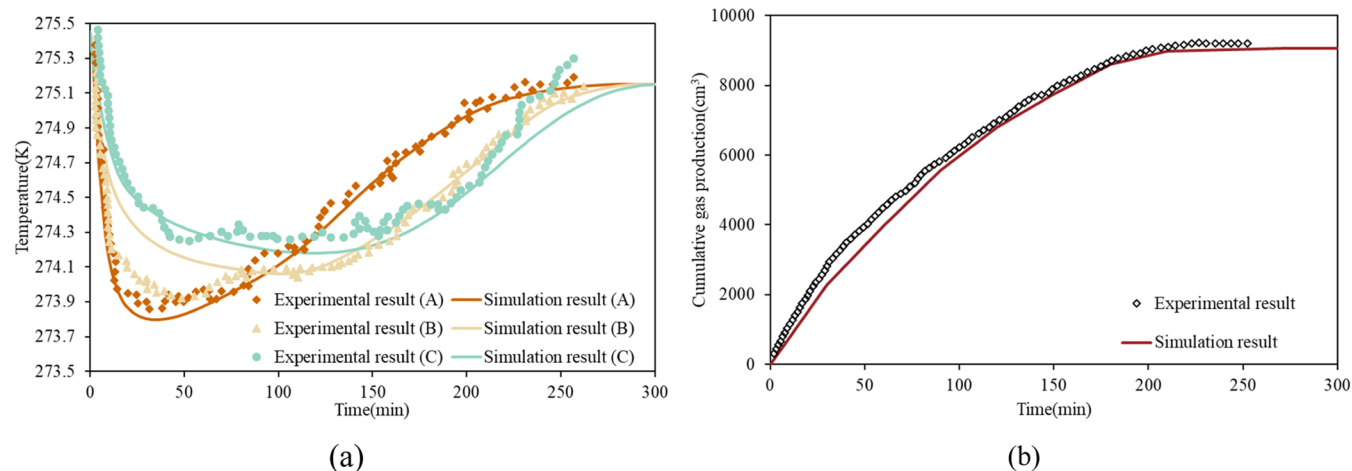
2.3. Simulation Model. The numerical simulation model is constructed based on the geologic system representing the site in the Shenhu area of the SCS, as shown in Figure 4. The 2D axisymmetric simulation model has dimensions of 100 m × 207 m, with 22 m allocated for the NGH formation, 155 m for the overlying formation, and 30 m for the underlying formation. The hydrate saturation of NGH formation in this model is 0.438, and the seafloor is located at a depth of 1108 m. The initial pore pressure field, initial temperature field, and initial stress field are calculated through hydrostatic pressure, geothermal gradient, and lithostatic pressure at the corresponding depth, respectively. The physical fields described above are set within the entire model. The upper boundary is subject to a hydrostatic pressure boundary condition, while the right and bottom boundaries are constrained in terms of normal displacement during the analysis.

This study consists of two stages in the model calculation process. In stage one, an in situ stress balance is conducted to attain a stable state for the entire model prior to hydrate production. This stage ensures that the model is in equilibrium. In stage two, the bottom hole pressure for the vertical production well is set to 5.83 MPa and remains unchanged to induce hydrate decomposition and simulate the process of hydrate depressurization. In addition, the main parameters are shown in Table 2.

3. RESULTS AND ANALYSIS

3.1. Production Dynamic Analysis. Figure 5(a) presents the spatial distribution of pore pressure within the NGH formation under varying durations of depressurization. It can be observed that the pore pressure experiences a significant decrease during the depressurization process. As the duration of depressurization increases, the zone where the pressure declines expands. Furthermore, it is noteworthy that the rate of pressure propagation demonstrates notable variations during the initial stages of depressurization, gradually decreasing as

(a)

(b)

Figure 3. Comparison between the numerical simulation results and the experimental data: (a) temperature at test points and (b) cumulative gas production.
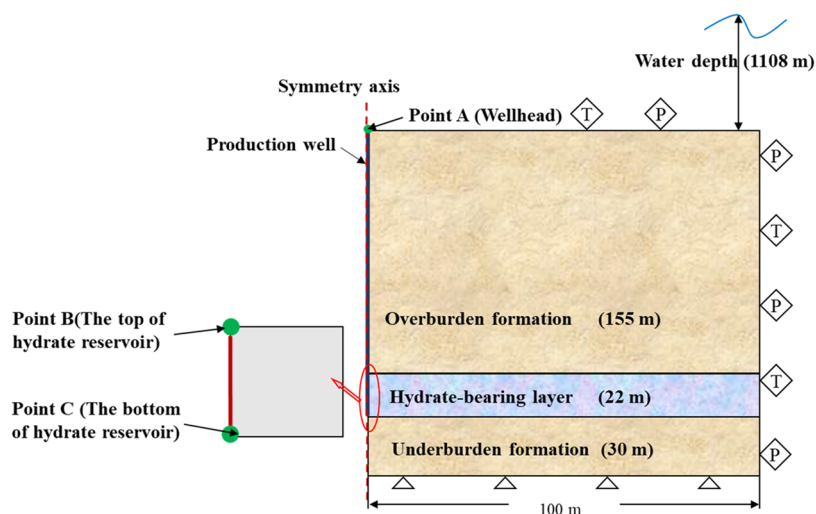
Figure 4. Schematic diagram of the geometric model.

Table 2. Main Parameters for Numerical Simulations[47−49]

parameters	value	parameters	value
depth of water	1108 m	water density	1000 kg·m^{-3}
NGH density	910 kg·m^{-3}	rock grain density	2200 kg·m^{-3}
water thermal conductivity	0.6 W·m^{-1}·K^{-1}	water specific heat	4.2 kJ·kg^{-1}·K^{-1}
rock grain thermal conductivity	1.5 W·m^{-1}·K^{-1}	rock grain specific heat	1.6 kJ·kg^{-1}·K^{-1}
NGH thermal conductivity	0.4 W·m^{-1}·K^{-1}	NGH specific heat	2.1 kJ·kg^{-1}·K^{-1}
gas thermal conductivity	0.00335 W·m^{-1}·K^{-1}	gas specific heat	2.093 kJ·kg^{-1}·K^{-1}
permeability within overlying formation and underlying formation	10 mD	initial permeability within NGH formation	75 mD
initial porosity	0.41	geothermal gradient	0.0456 K·m^{-1}
initial pressure at the base of NGH formation	13.83 MPa	residual gas saturation	0.05
initial temperature at the base of NGH formation	287.4 K	irreducible water saturation	0.3
production pressure difference	7 MPa	production time	600 days
n	6	N	5
ng	3	nw	5

the duration progresses. This indicates that the initial response to depressurization is characterized by a higher speed compared with the later stages.

Figure 5(b) presents the spatial distribution of NGH saturation within the formation under different durations of production. Due to the variations in formation temperature and pore pressure, hydrates gradually dissociated into methane gas and water. It is evident that hydrate dissociation initiates in close proximity to the production well, and the extent of hydrate dissociation expands as the production duration increases. For instance, the dissociation front of hydrates at the middle location of the formation is positioned 9.4 m away from the wellbore after 100 days of production; this dissociation front has extended to a distance of 16.6 m after 600 days of production.

Additionally, a notable difference can be observed in the extent of hydrate dissociation between the lower and upper sections of the formation. This discrepancy can be attributed to the impact of pressure differentials during production. The relatively higher-temperature fluids originating from the underlying formations ascend and engage in heat exchange with the bottom part of the formation, resulting in an elevated temperature in that region. As a consequence, the rate of hydrate dissociation is accelerated in the lower section. This phenomenon is clearly manifested in the spatial distribution of

temperature within the formation under different durations of production, as shown in Figure 5(c).

Figure 5(d), (e) present the spatial distribution of water and gas saturation within the formation under various durations of production, respectively. It can be observed that during production, the water saturation in the hydrate dissociation region experiences a significant increase, and the water saturation in the upper and lower part of the formation is higher than that in the middle part. This can be attributed to the release of water during hydrate decomposition, as well as the external fluids from the overlying and underlying formations enter the NGH formation through interconnected pathways driven by the pore pressure differentials and flow toward the wellbore.

At the same time, due to the existence of capillary force, a large amount of water occupies the flow channel of the gas, resulting in lower gas saturation in the upper and lower parts of the NGH formation. The gas saturation distribution also reveals the migration of gas generated from hydrate dissociation toward the wellbore. As the dissociation front of the hydrate advances away from the well, the distance that methane gas needs to migrate also increases. Consequently, the gas faces greater resistance to its production, which hampers the efficiency of the hydrate production.

Figure 5(f) illustrates the spatial distribution of vertical displacements within the formation at various production
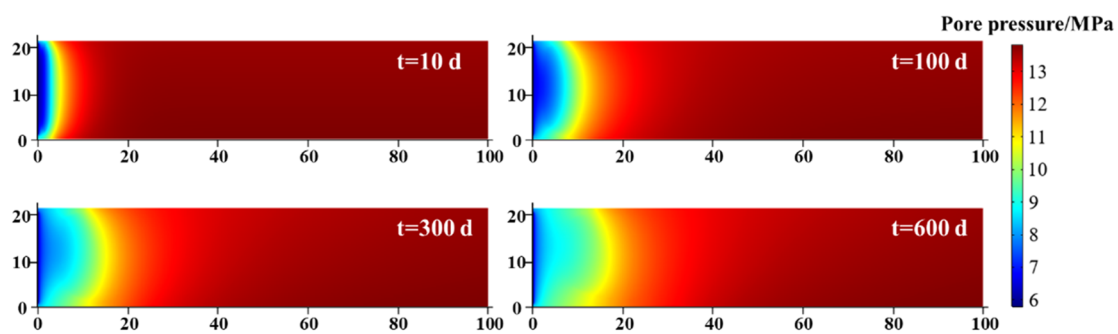
(a)
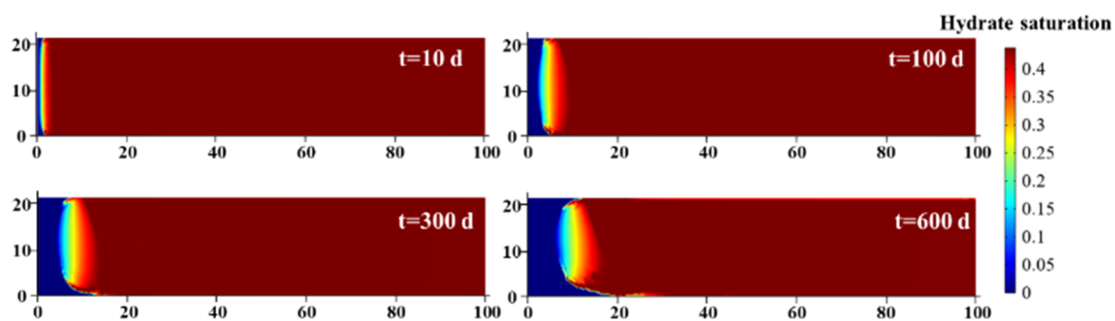
(b)
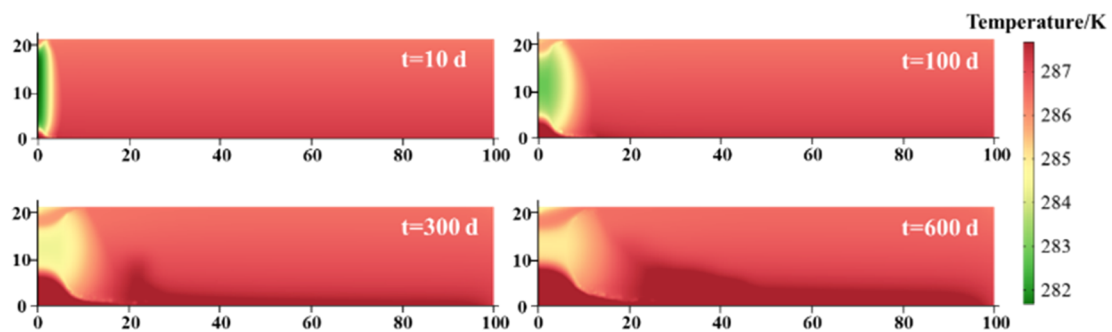
(c)
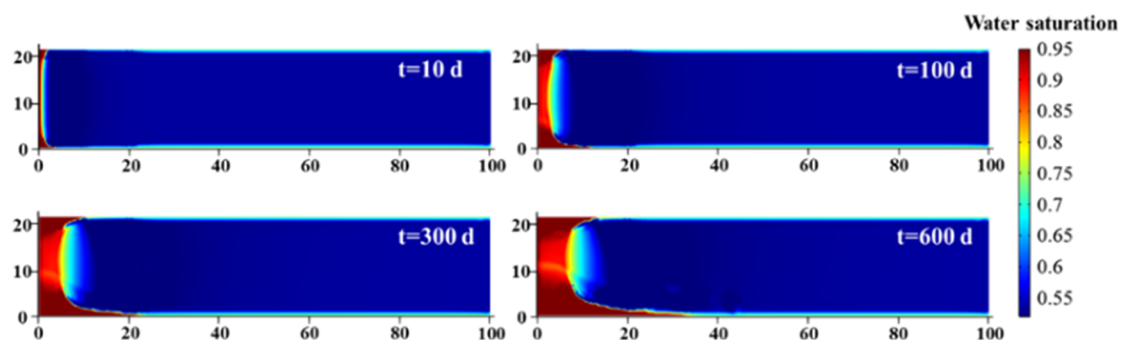
(d)

Figure 5. continued
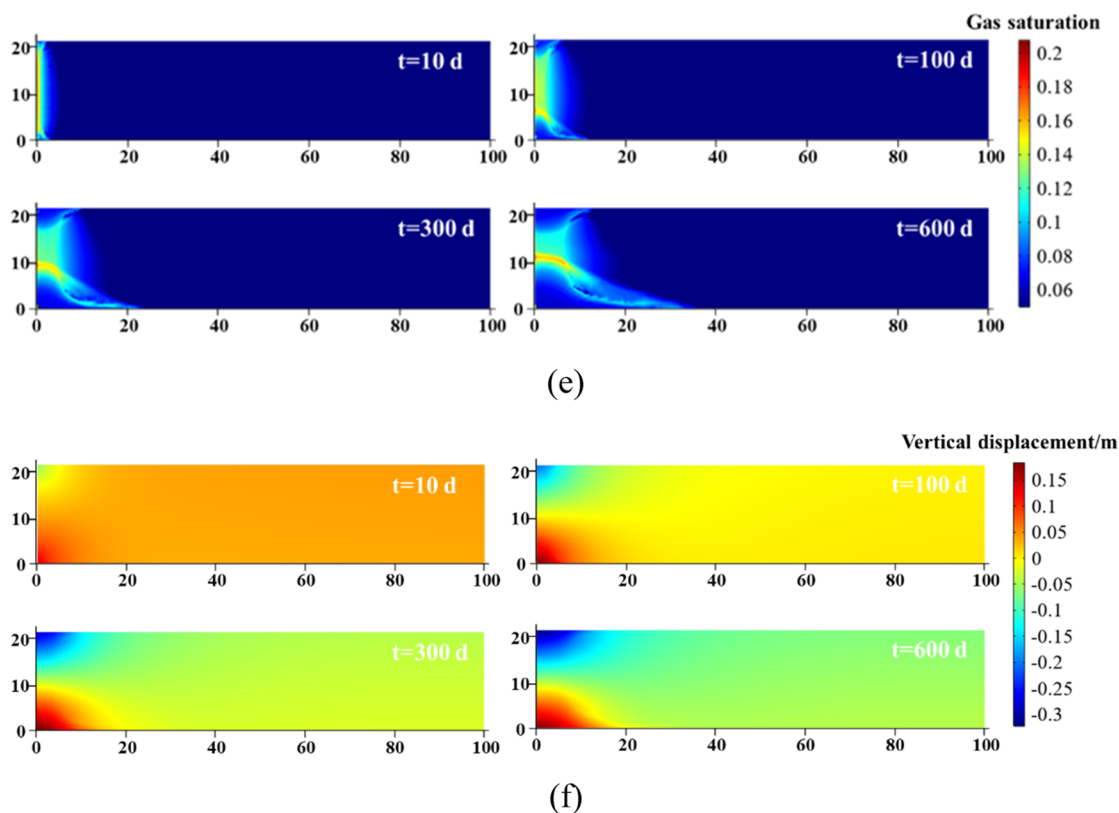
Figure 5. Evolution of the typical physical properties at the NGH formation over time: (a) pore pressure, (b) hydrate saturation, (c) temperature, (d) water saturation, (e) gas saturation, and (f) vertical displacement.
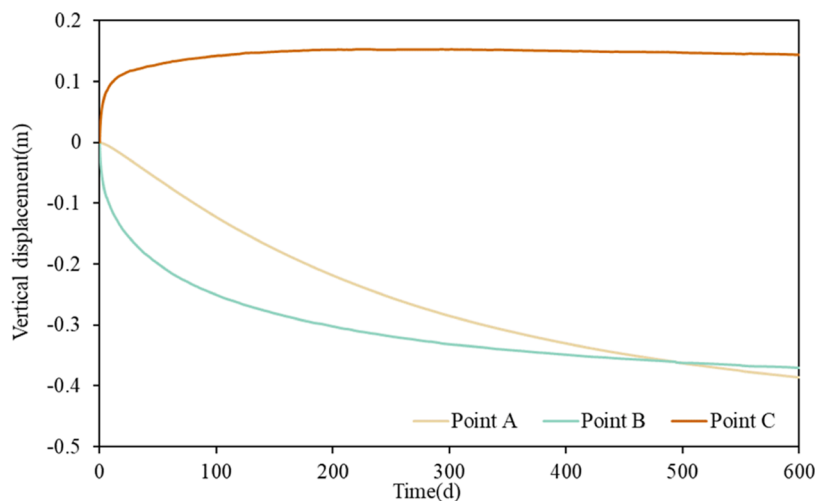
Figure 6. Variation of vertical displacement at test points.

durations. The region experiencing hydrate dissociation undergoes compression due to the reduction in mechanical properties and the increase in effective stress. This leads to subsidence in the overlying formation, while uplift is observed in the underlying formation. As the production time increases, the compression within the reservoir intensifies, as shown in Figure 6. Specifically, after 100 days of production, point B (at the top of the formation) exhibits a subsidence of approximately 0.250 m, while point C (at the bottom of the formation) uplifts around 0.143 m. After 600 days of production, the subsidence at point B increases to 0.370 m, and the uplift at point C increases to 0.145 m. The vertical

displacement trend at point A (the wellhead) follows a similar displacement trend to points B and C, with the rate of change gradually decreasing as the production time progresses.

3.2. Influence of Mechanical Behavior on Hydrate Production. To further analyze the impact of stress field on hydrate production, a coupled thermal-hydraulic-chemical (THC) model was developed, excluding solid mechanics considerations. Figure 7 shows the gas production behaviors over a 600 day depressurization process. Notably, when accounting for the effect of stress-induced changes in the formation's pore structure, both the gas production rate and cumulative gas production are lower compared to the scenario,
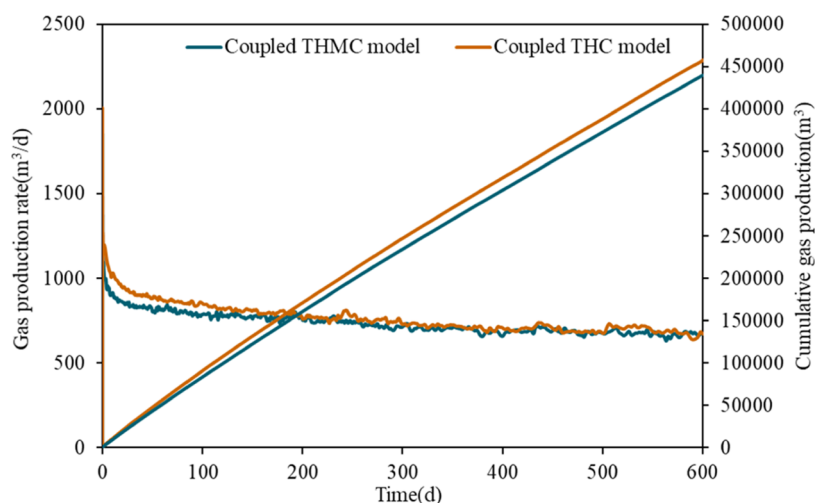
Figure 7. Comparison of production characteristics with the THMC model and THC model.
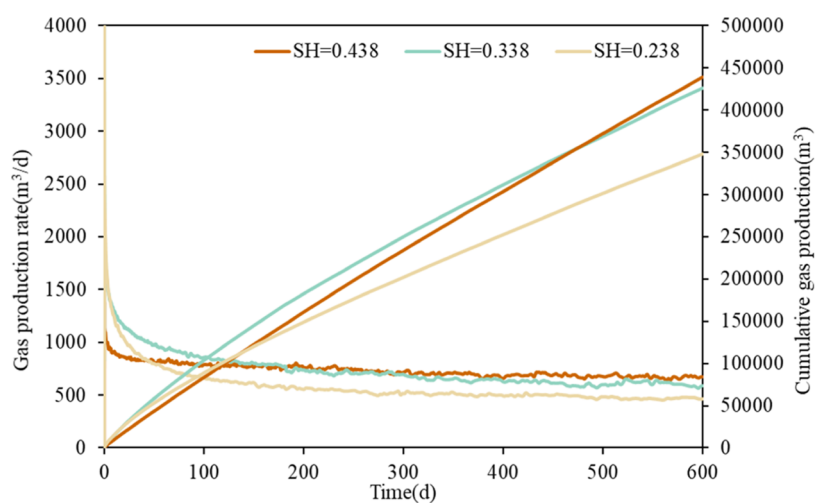
Figure 8. Comparison of production characteristics with different hydrate saturations.

where solid mechanics effects are not considered. Hence, neglecting the effects of solid mechanics in the analysis of hydrate formation productivity can result in underestimated assessment results, particularly in the initial stages of production. Accounting for solid mechanics effects allows for a more accurate prediction of the gas production capacity and yields more reliable assessment outcomes. Additionally, considering the influence of solid mechanics provides a comprehensive understanding of the geomechanical behavior associated with hydrate reservoirs.

3.3. Influence of Natural Gas Hydrate Saturation. The initial saturation of NGH is a crucial factor affecting reservoir exploitation along with the initial flow parameters and mechanical properties of the formation. These factors collectively influence the gas productivity and formation stability. In this section, we developed a hydrate formation productivity calculation model to analyze the impact of different initial saturation conditions. The model maintained consistent conditions with the initial model while varying the initial hydrate saturations to values of 0.238, 0.338, and 0.438, respectively.

Figure 8 shows the temporal evolution of gas production behaviors under different initial hydrate saturation conditions. It can be observed that during the early stages of production, a higher initial hydrate saturation corresponds to lower gas production rates under identical production conditions. However, as the production process progresses, the gas production rate for low saturation conditions exhibits a gradual decline, eventually dropping below the rate observed for higher saturation conditions.

This phenomenon can be explained by the initial permeability of NGH, which is higher under lower hydrate saturation conditions. As a result, the gas generated from hydrate dissociation tends to flow more readily toward the wellbore under the same production pressure differential, leading to a higher initial gas production rate. However, as time progresses, the reservoir with a higher initial hydrate saturation retains a greater amount of hydrate content. At the same time, advancement of the hydrate dissociation front becomes relatively limited, resulting in a shorter distance for the released gas to travel to reach the wellbore. Both of these factors contribute to a smaller decrease in the gas production rate in high-saturation hydrate formation, resulting in a higher gas production rate in the later stages of production compared with low-saturation hydrate formation. The trend in cumulative gas production further corroborates the aforementioned observation. Specifically, at a production time of 480 days, the cumulative gas production from an initial hydrate saturation of
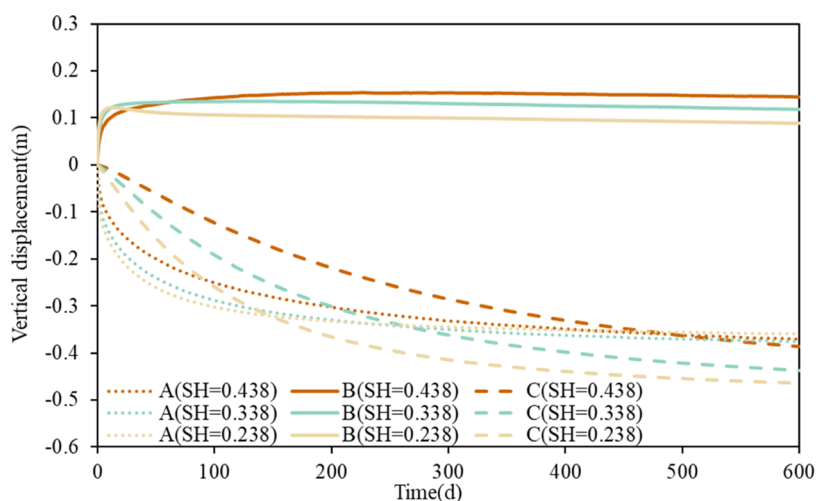
Figure 9. Comparison of vertical displacement at test points with different hydrate saturations.
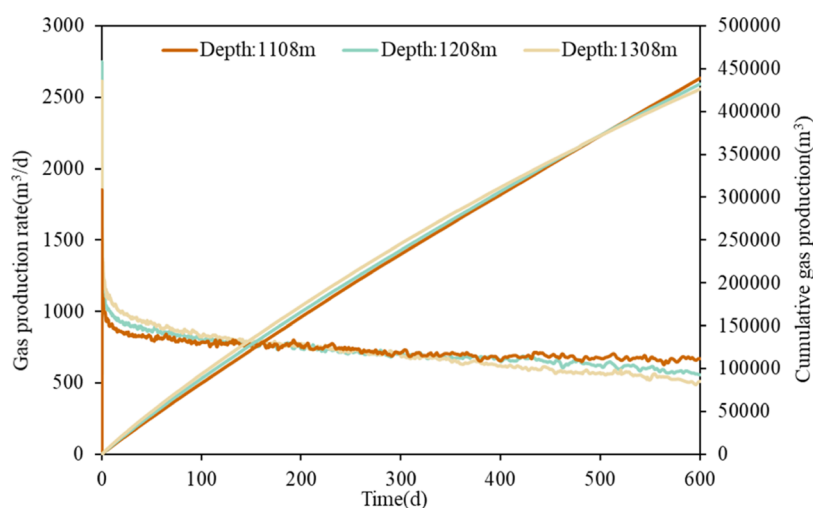
Figure 10. Comparison of production characteristics with different seawater depths.

0.438 is equivalent to the cumulative gas production from an initial saturation of 0.338. However, as the production duration extends beyond this point, the cumulative gas production from an initial saturation of 0.438 gradually surpasses that from an initial saturation of 0.338.

Figure 9 shows the vertical displacement evolution of points A−C under different initial hydrate saturation conditions. It is observed that higher hydrate saturation leads to larger vertical displacements of points B and C under the same production time conditions, indicating that the overall compression of the formation is more pronounced under conditions of higher hydrate saturation. The underlying reason can be attributed to the higher initial elastic modulus and other mechanical properties of the reservoir under high hydrate saturation conditions. As the production process progresses and hydrate decomposition occurs, the changes in mechanical properties become more pronounced. The higher initial elastic modulus accentuates the weakening of the formation, thereby amplifying the vertical displacements.

It also can be observed that there is a negative correlation between the vertical displacement at point A and the hydrate saturation. In other words, the higher is the initial hydrate saturation, the smaller is the subsidence at the wellhead. This is because the formation characterized by high hydrate saturation

exhibits elevated mechanical properties, which effectively mitigate the deformation of overlying formation and reduce the subsidence at the wellhead.

3.4. Influence of Seawater Depth. The variation in seawater depth will impact the initial pore pressure in the formation, as well as the fluid flow behavior within the formation. In this section, we established a hydrate reservoir productivity calculation model to analyze the effects of different seawater depths. While maintaining consistency with other conditions, three distinct seawater depths were selected: 1108, 1208, and 1308 m.

Figure 10 shows the evolution of the gas production rate and cumulative gas production at varying seawater depths. It can be observed that in the early stages of production, the formation located at deeper seawater depths exhibited a higher production rate. However, as time progressed, its production rate gradually decreased and eventually became lower than those of the formation at shallower seawater depths. Furthermore, during the long-term production period, the cumulative gas production of the formation at shallower seawater depths accumulates a greater volume of natural gas compared to reservoirs at greater seawater depths.

A greater seawater depth leads to a higher reservoir pore pressure. This leads to a larger pressure gradient or production
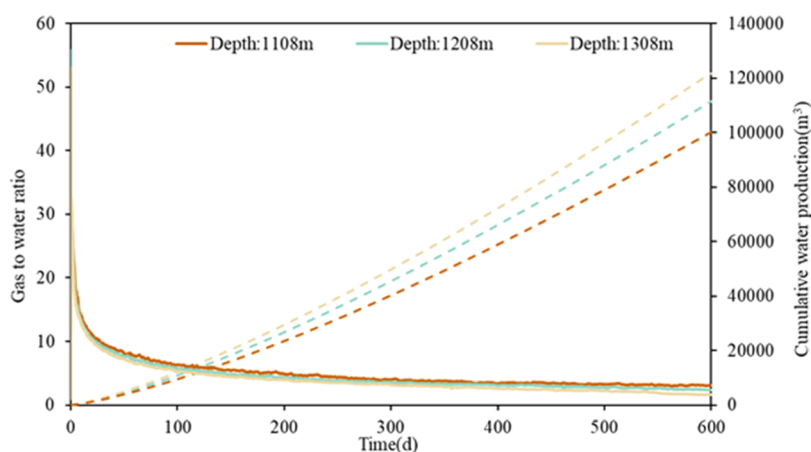
Figure 11. Comparison of gas-to-water ratio and cumulative water production with different seawater depths.
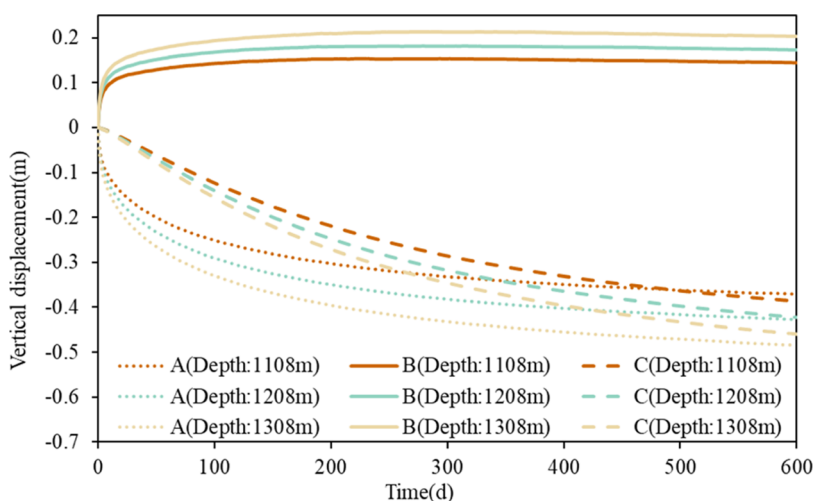
Figure 12. Comparison of vertical displacement at test points with different seawater depths.

pressure differential between the formation and the wellbore under the same bottom hole pressure conditions. A larger production pressure differential leads to higher decomposition rates, resulting in higher gas production rates in the early stages of production. Moreover, the larger production pressure differential enhances the flow of gas toward the wellbore, increasing the gas migration velocities within the formation, further contributing to higher initial production rates.

As the production time increases and hydrates near the wellbore are depleted, a different phenomenon occurs. The pressure differential, along with the capillary forces within the porous media, facilitates the movement of water toward the wellbore. This leads to an increase in water production from the formation, while the production of natural gas gradually decreases.

This phenomenon can also be observed in Figure 11. The gas-to-water ratio (GWR) in the formation exhibits a consistent higher value under lower seawater depth conditions compared to greater seawater depth conditions. Additionally, the cumulative water production is lower under lower seawater depth conditions.

Figure 12 depicts the variation of vertical displacements over time for points A–C under different seawater depth conditions. It can be observed that the magnitude of vertical displacements at these points exhibits a positive correlation

with seawater depth. As the seawater depth increases, both the compression of the NGH formation and the subsidence at the wellhead become more pronounced.

This phenomenon can be attributed to the simulation assuming a constant bottom hole pressure during production. Therefore, under a greater seawater depth, the formation experiences a higher pore pressure, which in turn leads to a larger pressure differential between the reservoir and the well. This significant pressure differential induces substantial changes in the effective stress during the production process. As a result, the formation undergoes heightened compression, leading to increased vertical displacement and amplified subsidence at the wellhead. In simpler terms, the higher seawater depth causes greater pore pressure and pressure differentials, leading to a more significant deformation and subsidence of the reservoir.

4. CONCLUSIONS

A two-dimensional axisymmetric numerical model was established to simulate hydrate reservoir production by depressurization through a vertical well. The effects of mechanical properties on hydrate production were analyzed; mechanical behavior and production data were analyzed under different initial hydrate saturations and seawater depths. The conclusions are as follows:

(1) When considering the influence of stress field on formation pore structure, the gas production rate and cumulative gas production are all lower than that without considering the influence of solid mechanics, and this difference is especially significant in the initial stage of production.

(2) Higher initial hydrate saturation leads to lower gas production rates in the early stages of production; as production progresses, reservoirs with higher initial hydrate saturation retain more hydrate content and exhibit a smaller decrease in gas production rate, leading to higher gas production rates in the later stages of production compared to low-saturation reservoirs.

(3) As the production process advanced, the decomposition of hydrates induced changes in mechanical properties, with the higher initial elastic modulus intensifying the reservoir's weakening and amplifying vertical displacements. Higher hydrate saturation signifies enhanced reservoir compression compared to lower saturation conditions. Additionally, a negative correlation was observed between the subsidence at the wellhead and hydrate saturation.

(4) Deeper seawater depth initially yielded higher gas production rate, but as time progressed, the rates gradually decreased and fell below that of shallower seawater depths. In the long term, reservoirs at shallower depths accumulated a greater volume of natural gas. Moreover, as the depth of seawater increases, both reservoir compression and wellhead subsidence intensify.

■ AUTHOR INFORMATION

Corresponding Author

Yuanfang Cheng — *School of Petroleum Engineering, China University of Petroleum (East China), Qingdao 266580, China;* ⊙ orcid.org/0009-0008-0630-7798; Email: yfcheng@126.com

Authors

Mingyu Xue — *School of Petroleum Engineering, China University of Petroleum (East China), Qingdao 266580, China*

Yang Li — *Sinopec Research Institute of Petroleum Engineering Co., Ltd., Beijing 102206, China*

Chuanliang Yan — *School of Petroleum Engineering, China University of Petroleum (East China), Qingdao 266580, China*

Zhongying Han — *School of Petroleum Engineering, China University of Petroleum (East China), Qingdao 266580, China;* ⊙ orcid.org/0000-0002-0034-3578

Yong Chen — *School of Petroleum Engineering, China University of Petroleum (East China), Qingdao 266580, China*

Bo Sun — *School of Petroleum Engineering, China University of Petroleum (East China), Qingdao 266580, China;* ⊙ orcid.org/0000-0001-8466-5533

Complete contact information is available at: https://pubs.acs.org/10.1021/acsomega.3c05484

Author Contributions

Methodology, conceptualization, supervision (Y.C., C.Y., and Z.H.), software, investigation, formal analysis (M.X., Y.C., Y.L., and B.S.), writing—review and editing (M.X.). All authors contributed critically to draft revision. All authors have read and agreed to the published version of the manuscript.

■ REFERENCES

(1) Sloan, E. D., Jr Fundamental principles and applications of natural gas hydrates. *Nature* **2003**, *426* (6964), 353–359.

(2) Kvenvolden, K. A.; Lorenson, T. D. The global occurrence of natural gas hydrate. *Nat. Gas Hydrates* **2001**, *124*, 3–18, DOI: 10.1029/GM124p0003.

(3) Yan, C.; Chen, Y.; Tian, W.; Cheng, Y.; Li, Y. Effects of methane-carbon dioxide replacement on the mechanical properties of natural gas hydrate reservoirs. *J. Cleaner Prod.* **2022**, *354*, No. 131703.

(4) Makogon, Y. F. Natural gas hydrates—A promising source of energy. *J, Nat. Gas Sci. Eng.* **2010**, *2* (1), 49–59.

(5) Klauda, J. B.; Sandler, S. I. Global distribution of methane hydrate in ocean sediment. *Energy Fuels* **2005**, *19* (2), 459–470.

(6) Sloan, E. D. Gas hydrates: review of physical/chemical properties. *Energy Fuels* **1998**, *12* (2), 191–196.

(7) Yin, Z.; Khurana, M.; Tan, H. K.; Linga, P. A review of gas hydrate growth kinetic models. *Chem. Eng. J.* **2018**, *342*, 9–29.

(8) Yu, Y. S.; Zhang, X.; Liu, J. W.; Lee, Y.; Li, X. S. Natural gas hydrate resources and hydrate technologies: a review and analysis of the associated energy and global warming challenges. *Energy Environ. Sci.* **2021**, *14* (11), 5611–5668.

(9) Yang, L.; Liu, Y.; Zhang, H.; Xiao, B.; Guo, X.; Wei, R.; Li, Y.; et al. The status of exploitation techniques of natural gas hydrate. *Chin. J. Chem. Eng.* **2019**, *27* (9), 2133–2147.

(10) Wang, H.; Wu, P.; Li, Y.; Liu, W.; Pan, X.; Li, Q.; He, Y.; Song, Y. Gas permeability variation during methane hydrate dissociation by depressurization in marine sediments. *Energy* **2023**, *263*, No. 125749.

(11) Chen, L.; Feng, Y.; Okajima, J.; Komiya, A.; Maruyama, S. Production behavior and numerical analysis for 2017 methane hydrate extraction test of Shenhu, South China Sea. *J. Nat. Gas Sci. Eng.* **2018**, *53*, 55–66.

(12) Koh, C. A.; Sum, A. K.; Sloan, E. D. State of the art: Natural gas hydrates as a natural resource. *J. Nat. Gas Sci. Eng.* **2012**, *8*, 132–138.

(13) Oyama, A.; Masutani, S. M. A review of the methane hydrate program in Japan. *Energies* **2017**, *10* (10), No. 1447, DOI: 10.3390/en10101447.

(14) Boswell, R. Japan completes first offshore methane hydrate production test—methane successfully produced from deepwater hydrate layers. *Center for Natural Gas and Oil* **2013**, *412* (1), 386–7614.

(15) Yamamoto, K.; Wang, X. X.; Tamaki, M.; Suzuki, K. The second offshore production of methane hydrate in the Nankai Trough and gas production behavior from a heterogeneous methane hydrate reservoir. *RSC Adv.* **2019**, *9* (45), 25987–26013.

(16) Li, J. F.; Ye, J. L.; Qin, X. W.; Qiu, H. J.; Wu, N. Y.; Lu, H. L.; Kou, B. B.; et al. The first offshore natural gas hydrate production test in South China Sea. *China Geol.* **2018**, *1* (1), 5–16.

(17) Sahu, C.; Kumar, R.; Sangwai, J. S. Comprehensive review on exploration and drilling techniques for natural gas hydrate reservoirs. *Energy Fuels* **2020**, *34* (10), 11813–11839.

(18) Ye, J. L.; Qin, X. W.; Xie, W. W.; Lu, H. L.; Ma, B. J.; Qiu, H. J.; Bian, H.; et al. The second natural gas hydrate production test in the South China Sea. *China Geol.* **2020**, *3* (2), 197–209.

(19) Cui, Y.; Lu, C.; Wu, M.; Peng, Y.; Yao, Y.; Luo, W. Review of exploration and production technology of natural gas hydrate. *Adv. Geo-Energy Res.* **2018**, *2* (1), 53−62.

(20) Wei, W. N.; Li, B.; Gan, Q.; Li, Y. L. Research progress of natural gas hydrate exploitation with CO₂ replacement: A review. *Fuel* **2022**, *312*, No. 122873.

(21) Liu, S.; Li, H.; Wang, B.; Sun, B. Accelerating gas production of the depressurization-induced natural gas hydrate by electrical heating. *J. Pet. Sci. Eng.* **2022**, *208*, No. 109735.

(22) Zhang, P.; Zhang, Y.; Zhang, W.; Tian, S. Numerical simulation of gas production from natural gas hydrate deposits with multi-branch wells: influence of reservoir properties. *Energy* **2022**, *238*, No. 121738.

(23) Dong, L.; Li, Y.; Wu, N.; Wan, Y.; Liao, H.; Wang, H.; Leonenko, Y.; et al. Numerical simulation of gas extraction performance from hydrate reservoirs using double-well systems. *Energy* **2023**, *265*, No. 126382.

(24) Feng, Y.; Chen, L.; Suzuki, A.; Kogawa, T.; Okajima, J.; Komiya, A.; Maruyama, S. Enhancement of gas production from methane hydrate reservoirs by the combination of hydraulic fracturing and depressurization method. *Energy Convers. Manage.* **2019**, *184*, 194−204.

(25) Yoneda, J.; Masui, A.; Konno, Y.; Jin, Y.; Kida, M.; Katagiri, J.; Tenma, N. Pressure-core-based reservoir characterization for geo-mechanics: Insights from gas hydrate drilling during 2012−2013 at the eastern Nankai Trough. *Mar. Pet. Geol.* **2017**, *86*, 1−16.

(26) Yan, C.; Ren, X.; Cheng, Y.; Song, B.; Li, Y.; Tian, W. Geomechanical issues in the exploitation of natural gas hydrate. *Gondwana Res.* **2020**, *81*, 403−422.

(27) Rutqvist, J.; Moridis, G. J.; Grover, T.; Silpngarmlert, S.; Collett, T. S.; Holdich, S. A. Coupled multiphase fluid flow and wellbore stability analysis associated with gas production from oceanic hydrate-bearing sediments. *J. Pet. Sci. Eng.* **2012**, *92-93*, 65−81.

(28) Yoon, H. C.; Yoon, S.; Lee, J. Y.; Kim, J. Multiple porosity model of a heterogeneous layered gas hydrate deposit in Ulleung Basin, East Sea, Korea: A study on depressurization strategies, reservoir geomechanical response, and wellbore stability. *J. Nat. Gas Sci. Eng.* **2021**, *96*, No. 104321.

(29) Sun, X.; Mohanty, K. K. Kinetic simulation of methane hydrate formation and dissociation in porous media. *Chem. Eng. Sci.* **2006**, *61*, 3476−3495.

(30) Liu, X.; Liu, C.; Wu, J. Dynamic characteristics of offshore natural gas hydrate dissociation by depressurization in marine sediments. *Geofluids* **2019**, *2019*, No. 6074892.

(31) Sun, J.; Zhang, L.; Ning, F.; Lei, H.; Liu, T.; Hu, G.; Lu, H.; Lu, J.; Liu, C.; Jiang, G.; et al. Production potential and stability of hydrate-bearing sediments at the site GMGS3-W19 in the South China Sea: A preliminary feasibility study. *Mar. Pet. Geol.* **2017**, *86*, 447−473.

(32) Sun, J.; Ning, F.; Liu, T.; Li, Y.; Lei, H.; Zhang, L.; Cheng, W.; Wang, R.; Cao, X.; Jiang, G. Numerical analysis of horizontal wellbore state during drilling at the first offshore hydrate production test site in Shenhu area of the South China Sea. *Ocean Eng.* **2021**, *238*, No. 109614.

(33) Ertekin, T.; Abou-Kassem, J. H.; King, G. R. *Basic Applied Reservoir Simulation*; OnePrteo, 2001.

(34) Sun, S.; Yang, Z.; Gu, L.; Lin, H.; Zhang, C. Effect of bubbles on the gas−water migration during gas hydrate dissociation by depressurization. *Fuel* **2023**, *339*, No. 127429, DOI: 10.1016/j.fuel.2023.127429.

(35) Moridis, G. J. *User's Manual for the Hydrate v1. 5 Option of TOUGH+ v1. 5: A Code for the Simulation of System Behavior in Hydrate-Bearing Geologic Media (No. LBNL-6869E)*; Lawrence Berkeley National Lab.(LBNL): Berkeley, CA, USA; 2014.

(36) Freij-Ayoub, R.; Tan, C.; Clennell, B.; Tohidi, B.; Yang, J. A wellbore stability model for hydrate bearing sediments. *J. Pet. Sci. Eng.* **2007**, *57*, 209−220.

(37) Liu, X.; Sun, Y.; Guo, T.; Rabiei, M.; Qu, Z.; Hou, J. Numerical simulations of hydraulic fracturing in methane hydrate reservoirs

based on the coupled thermo-hydrologic-mechanical-damage (THMD) model. *Energy* **2022**, *238*, No. 122054.

(38) Selim, M. S.; Sloan, E. D. Heat and mass transfer during the dissociation of hydrates in porous media. *AIChE J.* **1989**, *35*, 1049−1052.

(39) Chibura, P. E.; Zhang, W.; Luo, A.; Wang, J. A review on gas hydrate production feasibility for permafrost and marine hydrates. *J. Nat. Gas Sci. Eng.* **2022**, *100*, No. 104441.

(40) Rutqvist, J.; Moridis, G. J.; Grover, T.; Collett, T. Geo-mechanical response of permafrost-associated hydrate deposits to depressurization-induced gas production. *J. Pet. Sci. Eng.* **2009**, *67* (1−2), 1−12.

(41) Kim, H. C.; Bishnoi, P. R.; Heidemann, R. A.; Rizvi, S. S. Kinetics of methane hydrate decomposition. *Chem. Eng. Sci.* **1987**, *42* (7), 1645−1653.

(42) Wang, Q.; Wang, Z.; Li, P.; Song, Y.; Wang, D. Numerical modeling of coupled behavior of gas production and mechanical deformation of gas hydrate reservoir in Shenhu area, South China Sea: Enlightenments for field monitoring and model verification. *Energy* **2022**, *254*, No. 124406.

(43) Masuda, Y. In *Modeling and Experimental Studies on Dissociation of Methane Gas Hydrates in Berea Sandstone Cores*; Proceedings of the third international gas hydrate conference, 1999.

(44) Yin, Z.; Chong, Z. R.; Tan, H. K.; Linga, P. Review of gas hydrate dissociation kinetic models for energy recovery. *J. Nat. Gas Sci. Eng.* **2016**, *35*, 1362−1387.

(45) Deng, X.; Feng, J.; Pan, S.; Wang, Z.; Zhang, J.; Chen, W. An improved model for the migration of fluids caused by hydrate dissociation in porous media. *J. Pet. Sci. Eng.* **2020**, *188*, No. 106876.

(46) Wang, B.; Fan, Z.; Zhao, J.; Lv, X.; Pang, W.; Li, Q. Influence of intrinsic permeability of reservoir rocks on gas recovery from hydrate deposits via a combined depressurization and thermal stimulation approach. *Appl. Energy* **2018**, *229*, 858−871.

(47) Li, G.; Moridis, G. J.; Zhang, K.; Li, X. S. In *Evaluation of the Gas Production Potential of Mrine Hydrate Deposits in the Shenhu Area of the South China Sea*; Offshore Technology Conference: OnePetro, 2010.

(48) Li, G.; Moridis, G. J.; Zhang, K.; Li, X. S. In *The Use of Huff and Puff Method in a Single Horizontal Well in Gas Production from Marine Gas Hydrate Deposits in the Shenhu area of the South China Sea*; International Oil and Gas Conference and Exhibition in China: OnePetro, 2010.

(49) Wei, J.; Cheng, Y.; Yan, C.; Li, Q.; Han, S.; Ansari, U. Decomposition prevention through thermal sensitivity of hydrate formations around wellbore. *Appl. Therm. Eng.* **2019**, *159*, No. 113921.